International Journal of Nanomedicine

Dovepress
Taylor & Francis Group

Open Access Full Text Article

ORIGINAL RESEARCH

Microwave-Responsive MnFe-Based Molybdenum Disulfide Nanoflowers for Enhanced Thermal-Dynamic-Chemo Synergistic Therapy in Bladder Cancer

Yadong Liu[1,2,*], Yaodong Chen[3,*], Shazhou Ye[1,*], Jiasheng Hu[1], Zhong Zheng[1], Kaining Lu[1], Wu Chen[3], Zejun Yan[1,4], Xingyi Li[5]

[1]Department of Urology, The First Affiliated Hospital of Ningbo University, Ningbo, Zhejiang, People's Republic of China; [2]State Key Laboratory of Ultrasound in Medicine and Engineering, The Second Affiliated Hospital of Chongqing Medical University, Chongqing, People's Republic of China; [3]Department of Ultrasonic Imaging, First Hospital of Shanxi Medical University, Taiyuan, Shanxi, People's Republic of China; [4]Zhejiang Engineering Research Center of Innovative Technologies and Diagnostic and Therapeutic Equipment for Urinary System Diseases, The First Affiliated Hospital of Ningbo University, Ningbo, Zhejiang, People's Republic of China; [5]Department of Ultrasonic Imaging, The First Affiliated Hospital of Ningbo University, Ningbo, Zhejiang, People's Republic of China

*These authors contributed equally to this work

Correspondence: Xingyi Li; Zejun Yan, Email fyylixingyi@nbu.edu.cn; fyyyanzejun@nbu.edu.cn

Background: The most challenging clinical characteristic of bladder cancer (BC) is its exceptionally high recurrence rate. Recurrence, metastasis and drug resistance remain critical challenges in BC treatment. Microwave dynamic therapy (MWDT) is an emerging antitumor modality; however, its therapeutic efficacy is limited by the hypoxic tumor microenvironment (TME). To address these limitations, we developed a multifunctional nanoplatform (Mn-Fe-Dox-BSA-MoS_2) to enhance oxygenation and therapeutic efficiency. In this system, MoS_2 served as a microwave sensitizer and photoacoustic imaging (PAI) agent, while bovine serum albumin (BSA) improved biocompatibility. Doxorubicin (Dox) acted as a chemotherapeutic drug, Mn/Fe ion complexes provided catalase-like activity, and Cy5.5 enabled fluorescence imaging (FI).

Methods: Reactive oxygen species (ROS) generation, oxygen production, imaging capability, and microwave/acid-responsive drug release were systematically evaluated. The antitumor efficacy and underlying mechanisms of Mn-Fe-Dox-BSA-MoS_2-mediated therapy were further evaluated in MB49 cells in vitro and in BALB/c nude mice in vivo.

Results: The nanoflowers exhibited excellent biosafety and efficient microwave sensitization, producing abundant ROS under MW irradiation. Dual-mode FI/PAI imaging enabled precise visualization of tumor accumulation. Mn/Fe complexes catalyzed H_2O_2 decomposition to continuously generate O_2, alleviating tumor hypoxia and enhancing MWDT efficacy. Meanwhile, Dox was effectively delivered and released in response to MW irradiation and acidic TME conditions. The synergistic effects of chemotherapy, MWDT, and microwave thermotherapy (MWTT) significantly inhibited tumor cell proliferation.

Conclusion: Mn-Fe-Dox-BSA-MoS_2 nanoflowers enable FI/PAI dual-modal imaging-guided multimodal therapy, demonstrating potent antitumor efficacy in a preclinical BC model.

Keywords: molybdenum disulfide, microwave dynamic therapy, microwave thermotherapy, chemotherapy, bladder cancer

Introduction

Bladder cancer (BC) is the most prevalent and lethal malignancy within the urinary system, with its incidence rates rising annually.[1] One of the most challenging clinical characteristics of BC is its exceptionally high recurrence rate. Approximately 50–80% of patients with non-muscle invasive bladder cancer (NMIBC) experience tumor recurrence within five years, and 10–30% eventually progress to muscle-invasive bladder cancer (MIBC). High-risk NMIBC

https://doi.org/10.2147/IJN.S587614
Received: 29 December 2025
Accepted: 20 March 2026
Published: 11 April 2026

Graphical Abstract

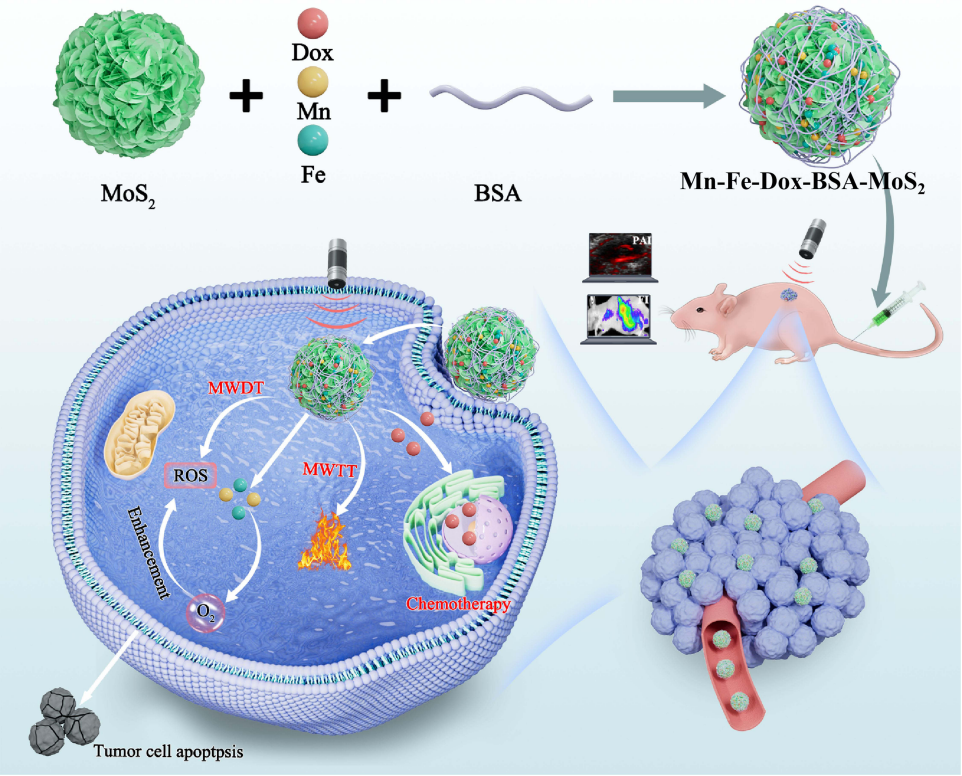

exhibits recurrence rates approaching 70–80%, and recurrent tumors frequently develop resistance to chemotherapy. The high recurrence rate of BC is attributed to tumor multifocality, field cancerization of the urothelium, tumor cell re-implantation during surgery, and the presence of occult residual lesions. In addition, epithelial–mesenchymal transition (EMT), cancer stem-like cell properties, and therapeutic selection pressure further contribute to tumor persistence and progression.[2,3] Currently, transurethral resection of bladder tumor (TURB) is the preferred treatment for NMIBC and radical cystectomy is regarded as the standard approach for MIBC.[4] Tumor cell implantation and the presence of residual primary lesions during TURB are key factors contributing to the high recurrence rate, often accompanied by complications such as bladder perforation and bleeding.[5] Additionally, the white-light cystoscopy employed during the procedure is ineffective in identifying small mucosal lesions, including carcinoma in situ and papillary carcinoma.[6] Radical cystectomy is a complex surgical procedure often associated with postoperative complications, such as infections and urinary fistulas, and urinary diversion significantly impacts patients' quality of life.[7,8] Given these challenges, early and comprehensive identification and removal of bladder cancer cells, along with inhibiting their invasive growth and distant metastasis, are crucial for improving patient prognosis and quality of life.

The emergence of nanotheranostics provides a novel approach to addressing these challenges.[9] By precisely modifying the size, shape, and surface properties of nanomaterials, it is possible to reduce their immunogenicity while simultaneously enhancing their biocompatibility, solubility, and targeting capabilities, enabling real-time intraoperative monitoring and navigation.[10] Currently, photodynamic therapy (PDT) and sonodynamic therapy (SDT) are widely used to enhance tumor therapeutic effect under real-time monitoring by multimodal imaging such as fluorescence, MRI, and ultrasound. However, the limited tissue penetration of PDT and the lack of targeting specificity in SDT restrict their clinical applications.[11] Hence, the development of innovative treatment modalities emerges as a crucial priority.

Microwaves (MW) are a form of energy composed of electric and magnetic fields, representing a type of electromagnetic wave with wavelengths ranging from 1 mm to 1 m (frequencies of 300 MHz to 300 GHz).[12] A wavelength of 2450 MHz is commonly used in clinical treatments.[13] Due to their ability to penetrate diverse types of tissues and non-metallic materials to a depth of approximately 5–7 cm, including water vapor, dehydrated tissues, and powdered materials, microwaves hold significant potential for the treatment of bladder cancer.[14] Microwave thermotherapy (MWTT) is a minimally invasive treatment for bladder cancer. It utilizes microwaves to increase the movement of charged particles and the rotation of water molecules, thereby elevating the temperature to achieve tumor ablation. This approach is distinguished by its deep tissue penetration, high thermal efficiency, and minimal side effects.[15,16] Nevertheless, the rates of tumor metastasis and recurrence remain high after MWTT. This is primarily due to the irregular shape or large size of tumors, which can hinder microwave heat from fully covering the entire tumor area.[17] Additionally, increasing the power of microwave thermotherapy excessively can lead to damage to surrounding normal tissues.[13] Incorporating the non-thermal effects of microwaves to target and eliminate residual tumor cells may further enhance the anticancer efficacy of MWTT.

Dynamic therapy can effectively kill tumor cells by generating reactive oxygen species (ROS) in situ, offering the benefits of high selectivity and minimal damage to surrounding normal tissues.[18] Microwave dynamic therapy (MWDT) is a specific form of dynamic therapy that generates ROS under microwave irradiation.[19] ROS encompass a variety of molecules, including singlet oxygen ($^1O_2$), superoxide anion radicals ($\cdot O_2^-$), hydrogen peroxide (H_2O_2), and hydroxyl radicals ($\cdot OH$).[13] When both tumor and normal cells are exposed to equivalent amounts of ROS, tumor cells, which typically have higher baseline levels of ROS, are more likely to reach the threshold for triggering apoptosis compared to normal cells. The minimum energy required to activate a substance to produce ROS is in the range of several hundred millivolts. In contrast, microwave energy is only 10^{-3} eV, which is insufficient to break chemical bonds or induce the generation of free radicals.[17] Therefore, to achieve the therapeutic effects of MWDT, appropriate microwave sensitizers are essential.

Molybdenum disulfide (MoS_2) is a transition metal sulfide with surface defects such as sulfur (S) and molybdenum (Mo) vacancies.[20] Combined with its large specific surface area, these characteristics endow MoS_2 with excellent microwave absorption properties. Even in the form of thin nanosheets, MoS_2 can efficiently absorb broadband microwaves.[21] Additionally, the interlayer spaces of MoS_2 are capable of retaining molecules or ions. Under MW irradiation, dipoles or ions align in the oscillating electric field, generating heat through molecular friction and dielectric loss.[21,22] Additionally, Wu et al successfully utilized MoS_2/Fe_3O_4 to mediate MWTT and MWDT for the treatment of deep bacterial-infected osteomyelitis. The MWDT functionality of MoS_2 can be attributed to its abundant surface defects and edge-active sites. These characteristics facilitate microwave-induced electron excitation and charge separation, where the excited electrons and holes interact with dissolved oxygen and water molecules to generate $\cdot O_2^-$, $\cdot OH$ and $^1O_2$.[21] In this study, we selected MoS_2 nanoflowers as the core nanocarrier. Compared to MoS_2 nanosheets, the MoS_2 nanoflowers exhibit a narrower size distribution, larger specific surface area, superior aqueous dispersibility, superior photothermal properties, and stronger light absorption capacity, while generating more ROS under MW irradiation. This is attributed to the higher specific surface area and interlayer structure of MoS_2 nanoflowers, which promote ion collisions, enhance MW energy conversion and absorption, and ultimately increase ROS generation.[23] Therefore, MoS_2 nanoflowers are ideal microwave-absorbing materials. To further enhance the biocompatibility and modifiability of MoS_2 nanoflowers, we employed bovine serum albumin (BSA) to encapsulate the nanoflowers. However, the tumor microenvironment (TME), characterized by hypoxia, weak acidity, and excessive H_2O_2, restricts the efficacy of MWDT.[18] Notably, hypoxia not only drives tumor drug resistance but also severely suppresses the generation of $^1O_2$. Continuous oxygen consumption during MWDT further aggravates intratumoral hypoxia. Therefore, remodeling the TME has the potential to enhance the therapeutic efficacy of MWDT. Moreover, BSA-MoS_2 has been proven to have excellent photoacoustic imaging (PAI) capabilities, enabling real-time monitoring of nanomaterial distribution in vivo and guiding optimal time windows for precise microwave therapy.[24] Considering the operational constraints of PAI in intraoperative environments, integrating fluorescence imaging (FI) capabilities to develop a dual-modal system could significantly improve its clinical applicability.

Invasive tumor cells are distributed in a scattered manner, making it difficult for microwave energy to effectively cover the entire tumor area, leading to tumor recurrence and metastasis.[25] Chemotherapy, in contrast, can overcome the limitations of the aforementioned microwave therapy. Doxorubicin (Dox) is a commonly used chemotherapeutic agent for treating tumors. It functions by intercalating into DNA, thereby inhibiting the activity of topoisomerase II.[26] This

inhibition, in turn, suppresses DNA replication, depriving tumor cells of their proliferative capacity and impeding cell cycle progression. However, the inherent cardiotoxicity of Dox limits its clinical application.[27] By utilizing nanomaterial-based targeting to deliver Dox directly to the tumor site in real-time, the drugs can diffuse freely within and around the tumor, effectively eliminating residual tumor cells.[28]

Herein, we have designed intelligent multifunctional nanomaterials (Mn-Fe-Dox-BSA-MoS_2) that are responsive to microwave and tumor microenvironments. The synergistic interactions among the components of the nanoflowers enable dual-modal imaging-guided MWDT, MWTT and Dox-based chemotherapy. This multimodal therapeutic strategy offers a novel strategy for bladder cancer treatment.

Materials and Methods

Materials

Manganese (II) chloride tetrahydrate ($MnCl_2{\cdot}4H_2O$), iron (III) chloride hexahydrate ($FeCl_3{\cdot}6H_2O$) and methylene blue (MB) were acquired from Sigma-Aldrich (Merck KGaA, Germany). Doxorubicin (Dox) was acquired from Aladdin Reagent Co., Ltd (Shanghai, China). Sodium molybdate and thiourea were obtained from Sinopharm Chemical Reagent Co., Ltd (Shanghai, China). The CCK-8 assay kit was purchased from Dojindo Laboratories (Kumamoto, Japan). Calcein AM/PI Test Kit, 1,1′-dioctadecyl-3,3,3′,3′-etramethylindocarbocyanine perchlorate (DiI) and Reactive Oxygen Species Assay Kit (DCFH-DA) were obtained from Beyotime Biotechnology (Shanghai, China). The Annexin V-FITC/PI Apoptosis Detection Kit was purchased from Multi Science (Hangzhou, China). Terminal deoxynucleotidyl transferase dUTP nick end labeling (TUNEL) kit was acquired from Elabscience Biotechnology Co., Ltd (Wuhan, China). The proliferating cell nuclear antigen (PCNA) antibody was acquired from Wuhan Sanying Biotechnology Co., Ltd (Wuhan, China). Bovine serum albumin (BSA) was purchased from Thermo Fisher Scientific (Waltham, MA, USA). BALB/c nude mice were purchased from the CAVENS Laboratory Animal Co., Ltd. (Changzhou, China).

Preparation of Mn-Fe-Dox-BSA-MoS_2 Nanoflowers

MoS_2 nanoflowers were synthesized hydrothermally by reacting sodium molybdate and thiourea (pH 1) at 180 °C for 24 h, followed by centrifugation, washing, and vacuum drying. The obtained MoS_2 was modified with BSA (1:3, w/w) under stirring for 2 h to yield BSA-MoS_2. Fe^{3+} and Mn^{2+} solutions were then mixed and incubated with BSA-MoS_2 at room temperature for 8 h to obtain Mn-Fe-BSA-MoS_2 after centrifugation and washing. Finally, Dox was loaded by incubating Mn-Fe-BSA-MoS_2 with Dox in aqueous solution in the dark for 24 h, and the Mn-Fe-Dox-BSA-MoS_2 nanoflowers were collected by centrifugation and washing.

The preparation of Cy5.5-labeled Mn-Fe-Dox-BSA-MoS_2 was carried out as follows. Initially, Cy5.5 was mixed with EDC in MES buffer (pH 5.5) and stirred for 30 minutes. The pH of the solution was then adjusted to 8.0, followed by the addition of NHS and Mn-Fe-Dox-BSA-MoS_2 nanoparticles. The mixture was stirred overnight, and the resulting product was collected by centrifugation.

Characterization of Nanoflowers

Transmission electron microscopy (TEM, Carl Zeiss SUPER-X, Germany) and scanning electron microscopy (SEM, Carl Zeiss SUPRA 55, Germany) were employed to visualize their surface morphology and microstructure. Elemental mapping and X-ray photoelectron spectroscopy (XPS, Thermo Fisher Scientific, USA) were performed to analyze the elemental composition and chemical states. The optical absorption properties were evaluated by UV-Vis-NIR spectroscopy (UV-3600, Shimadzu, Japan). The zeta potential was measured with a potentiometric analyzer (ZEN3690, UK). To evaluate biocompatibility, a hemolysis assay was conducted. Oxygen generation under MW irradiation was monitored with a dissolved-oxygen meter (ZEN3690, UK). The Micromeritics ASAP 2460 analyzer was used to determine the Brunauer-Emmett-Teller (BET) surface area and pore size of the material.

MWDT Performance Evaluation

Under light-protected conditions, BSA-MoS_2 nanoflowers were dissolved in deionized water and diluted to a concentration of 125 μg/mL. Subsequently, 30 μL of 1,3-diphenylisobenzofuran (DPBF, 1 mg/mL) solution was added to the nanoflower solution to prepare a 500 μL mixed system. The mixtures were then subjected to MW (5 W) for varying durations (1.5, 3, 4.5, 6, 7.5, and 9 minutes) in an ice bath. Following centrifugation, the supernatant was carefully collected, and its absorbance at 423 nm was measured using a spectrophotometer.

Furthermore, BSA-MoS_2 nanoflowers were dissolved in deionized water and diluted to concentrations of 500, 250, 125, 62.5, and 31.25 μg/mL. Then, 30 μL of DPBF was added to each nanoflower solution to prepare 500 μL of mixed solution. The mixtures were exposed to MW irradiation (5 W, 4.5 min) in an ice bath. After centrifugation, the supernatant was collected, and the absorbance at 423 nm was measured using a spectrophotometer.

To further investigate the impact of Mn and Fe ions on the MWDT, we used MB and DPBF as molecular probes to detect the generation of singlet oxygen ($^1O_2$) and hydroxyl radicals (·OH), respectively. The experiments comprised seven groups: control group, BSA-MoS_2 group, BSA-MoS_2+H_2O_2 group, Mn-Fe-BSA-MoS_2+H_2O_2 group, BSA-MoS_2 +MW group, BSA-MoS_2+H_2O_2+MW group, and Mn-Fe-BSA-MoS_2+H_2O_2+MW group. Following respective treatments according to the experimental design, absorbance measurements were conducted at 423 nm (for $^1O_2$ detection) and 664 nm (for ·OH detection) using a spectrophotometer.

MWTT Performance Evaluation

Deionized water, saline, and RPMI-1640 medium were individually exposed to microwave irradiation (5 W) for 9 minutes. Subsequently, Mn-Fe-Dox-BSA-MoS_2 nanoflowers were dissolved and diluted to 125 μg/mL in deionized water, saline, and RPMI-1640 medium, respectively. The solutions were then transferred to a 48-well plate (200 μL/well) and subjected to microwave irradiation (8 W) for 6 minutes. Temperature changes were monitored in real-time and recorded using an infrared thermal imager.

Photoacoustic Imaging in vitro

A 3% agarose gel was prepared as the imaging matrix. Mn-Fe-Dox-BSA-MoS_2 nanoflowers were dissolved in deionized water and serially diluted to concentrations of 1, 0.5, 0.25, 0.125, and 0.0625 mg/mL. 200 μL aliquots of each diluted nanoflower solution were loaded into separate wells of the agarose gel phantom. Then the samples were imaged using the Vevo LAZR Photoacoustic Imaging System.

Targeting Efficiency Assessment of Nanoflowers in vitro

To avoid spectral overlap between Dox and DiI, MB49 cells (Otwo Biotech Inc. cat #: HTX2716, Guangzhou, China) were sequentially incubated with the two probes. The phagocytosis of DiI-labeled Mn-Fe-BSA-MoS_2 was first visualized by fluorescence microscopy at designated time points (0.5, 1, 2, 4, and 6 hours), followed by the quantification of cellular uptake for DiI-labeled Mn-Fe-Dox-BSA-MoS_2 using flow cytometry at the corresponding intervals. In addition, bio-transmission electron microscopy confirmed that the nanoflowers had been internalized by MB49 cells.

Cytotoxicity Evaluation of Mn-Fe-BSA-MoS_2 Nanoflowers

HUVEC and MB49 cells were separately seeded in 96-well plates (8×10^3 cells/well) and treated with nanoflowers at varying concentrations (15.625–500 μg/mL) for 24 hours. Following incubation, the culture medium was aspirated and cells were washed twice with PBS. Subsequently, CCK-8 solution was added to each well and the plates were incubated in the dark at 37 °C for 1 hour. The absorbance was then measured at 450 nm using a microplate reader.

Cell Viability Assay

MB49 cells were seeded in 96-well plates (8×10^3 cells/well) and divided into the following groups: control group (N), MW group (performed in an ice bath), BSA-MoS_2+MW group (performed in an ice bath), Mn-Fe-BSA-MoS_2 group (performed in an ice bath), BSA-MoS_2+MW group, and Mn-Fe-BSA-MoS_2+MW group. After 4 hours of nanoflowers treatment (125 μg/mL), the culture medium was removed and cells were subjected to the respective interventions

according to the above groupings for 6 minutes. Following 24 hours of incubation, the medium was aspirated and cells were washed twice with PBS. CCK-8 solution was then added to each well, and the plates were incubated in the dark at 37 °C for 1 hour. Finally, the optical density was measured at 450 nm using a microplate reader.

Additionally, to evaluate the impact of Dox on cell viability, the cells were divided into the following groups: control (N), MW, Dox-BSA-MoS_2, Mn-Fe-Dox-BSA-MoS_2, Dox-BSA-MoS_2+MW, and Mn-Fe-Dox-BSA-MoS_2+MW. All groups received the corresponding interventions at room temperature, and cell viability was assessed using the method described above.

ROS Detection

MB49 cells were seeded in a 12-well plate at a density of 1×10^5 cells/well and divided into the following groups: control group (N), MW group, Dox-BSA-MoS_2 group, Mn-Fe-Dox-BSA-MoS_2 group, Dox-BSA-MoS_2+MW group, and Mn-Fe-Dox-BSA-MoS_2+MW group. After 24 hours, cells were treated according to the above groupings (125 μg/mL, 8 W) for 6 minutes. Following 4 hours of co-culture, the medium was removed, and the cells were washed twice with PBS. Subsequently, cells were incubated with serum-free RPMI-1640 medium containing the DCFH-DA probe (10 μmol/L) at 37 °C for 20 minutes. After incubation, cells were washed three times with serum-free medium to thoroughly remove any extracellular DCFH-DA. Finally, ROS generation was measured by flow cytometry.

Cell Apoptosis Analysis

MB49 cells were seeded in 6 cm plates (2×10^5 cells/well) and subjected to corresponding interventions. After washing and trypsinization, the cells were centrifuged and resuspended in pre-cooled PBS, followed by a second centrifugation. The cells were then resuspended in buffer and 100 μL of the cell suspension was transferred to a flow cytometry tube. Apoptosis dye was added, and the samples were analyzed by flow cytometry.

Live/Dead Cell Staining

MB49 cells were seeded in 3.5 cm culture dishes (1×10^5 cells/well). After 24 hours, the aforementioned nanoflowers (125 μg/mL) were added. Following six hours of incubation, the culture medium was removed and cells were washed twice with PBS. Then, 400 μL of culture medium was added, and the cells were subjected to microwave irradiation (8 W) for 6 minutes as described in the ROS experiment. After removing the medium and washing twice with PBS, 500 μL of Calcein AM/PI working solution was added, followed by incubation at 37 °C in the dark for 30 minutes. The staining solution was then removed, cells were washed twice with PBS, and 100 μL of PBS was added. Finally, cells were observed and imaged under a fluorescence microscope.

Assessment of Nanoflowers Biosafety in vivo

All experimental protocols in this study were strictly designed following the 3R principles (Replacement, Reduction, and Refinement) and conducted in accordance with the guidelines of the Animal Ethics Committee, and were formally approved by the animal ethics committee of the Second Affiliated Hospital of Chongqing Medical University (IACUC-SAHCOMU-2023-0004). All mice were anesthetized or euthanized using sodium pentobarbital (intraperitoneal injection, 50 mg/kg). Twenty-five healthy BALB/c mice were randomly divided into 5 groups: control group (N), 3-day treatment group, 7-day treatment group, 14-day treatment group, and 28-day treatment group. Each group of mice was intravenously injected via the tail vein with Mn-Fe-Dox-BSA-MoS_2 nanoflowers (1 mg/mL, 100 μL). Mice were euthanized on days 3, 7, 14, and 28 after injection. Blood was collected for routine blood tests, and serum was collected for biochemical analysis. Tissue samples from the heart, liver, spleen, lungs, and kidneys were collected for histopathological staining, and tissue conditions were observed under a microscope.

Pharmacokinetic Evaluation of Nanoflowers in vivo

Three BALB/c mice were intravenously injected with Mn-Fe-BSA-MoS_2 nanoflowers (1 mg/mL, 100 μL) via the tail vein. Blood samples (approximately 50 μL per time point) were collected from the retro-orbital venous plexus at

predetermined time intervals (0.5, 1, 3, 8, 24, and 48 hours) post-injection. Molybdenum (Mo) concentrations in blood were quantitatively analyzed by inductively coupled plasma optical emission spectrometry (ICP-OES).

Fluorescence and PA Imaging in vivo

BALB/c nude mice (n = 3) were intravenously injected with saline solution containing Mn-Fe-Dox-BSA-MoS_2 (1 mg/mL, 100 μL). Sequential photoacoustic images were acquired at predetermined time intervals (1, 3, 6, 9, 12, and 24 h post-injection) using a photoacoustic imaging system, followed by quantitative signal intensity analysis.

And BALB/c nude mice (n = 3) were intravenously injected with 100 μL of a saline solution containing Cy5.5-labeled Mn-Fe-Dox-BSA-MoS_2 at a concentration of 1 mg/mL. Fluorescence imaging was performed at 3, 6, 9, and 24 h post-injection using an in vivo imaging system. After 24 hours, the mice were euthanized, and tumor tissues along with major organs were harvested for subsequent ex vivo imaging.

MWTT Performance of Mn-Fe-Dox-BSA-MoS_2 Nanoflowers in vivo

Ten BALB/c nude mice were randomly divided into two groups. Subcutaneous tumor models were established on the dorsal flank of each mouse. Six hours after intravenous injection of equal volumes of NaCl solution and Mn-Fe-Dox-BSA-MoS_2 nanoflowers via the tail vein, the tumor regions were exposed to microwave irradiation. A thermal imaging infrared instrument was used to monitor and record the temperature at the tumor site in real time.

Antitumor Therapy in vivo

MB49 cells (5×10^5) suspended in 100 μL of PBS were subcutaneously injected into the flanks of BALB/c nude mice to establish tumor xenografts. After 7 days of logarithmic growth, twenty-five MB49 tumor-bearing nude mice were randomly divided into five groups: the control group (N), Mn-Fe-Dox-BSA-MoS_2 group, microwave (MW) treatment group, Dox-BSA-MoS_2+MW group, and Mn-Fe-Dox-BSA-MoS_2+MW group. On days 1 and 4, the Mn-Fe-Dox-BSA-MoS_2 group, Dox-BSA-MoS_2+MW group, and Mn-Fe-BSA-MoS_2+MW group were intravenously injected with the corresponding nanoflower solutions (1 mg/mL, 100 μL), while the control and MW groups were injected with saline only. Six hours post-injection, the mice in the MW group were irradiated with microwaves at 8 W for 5 minutes, whereas Dox-BSA-MoS_2+MW and Mn-Fe-BSA-MoS_2+MW groups were subjected to microwave irradiation at 8 W for 5 minutes under real-time temperature monitoring. During the 7-day observation period, the body weight of the mice was measured every other day. On the seventh day, all mice were euthanized, and tumor tissues were collected for weight and volume measurement and Hematoxylin and eosin (H&E) staining. Proliferation and apoptosis in tumor tissues were evaluated by immunohistochemistry for PCNA and TUNEL staining, respectively.

Statistical Analysis

Statistical analysis was conducted using SPSS 22.0 software. Data are presented as mean ± standard deviation (SD). Comparisons between two groups were performed using Student's *t*-test, while differences among multiple groups were assessed using one-way ANOVA. Statistical significance was set at $p < 0.05$.

Results and Discussion

Preparation and Characterization of Mn-Fe-Dox-BSA-MoS_2

BSA exhibits excellent biocompatibility and biodegradability, and contains a variety of functional groups, including amino, carboxyl, hydroxyl, and thiol groups, which can be used to chelate fluorescent probes.[29] Additionally, BSA-modified MoS_2 demonstrates enhanced tumor-targeting capability through the enhanced permeability and retention (EPR) effect for passive drug delivery. Mn-Fe-BSA-MoS_2 nanoflowers were successfully obtained and further characterized to confirm their morphology and composition. TEM and SEM images revealed that the MoS_2 exhibited a flower-like morphology (Figure 1A and B). Elemental mapping and energy-dispersive X-ray spectroscopy (EDS) analysis confirmed the successful adsorption of Mn and Fe elements onto the MoS_2 nanoflowers (Figure 1C and D). XPS further confirmed the chemical composition of the MoS_2 nanoflowers (Figure 1E). The full spectrum displayed

 https://doi.org/10.2147/IJN.S587614

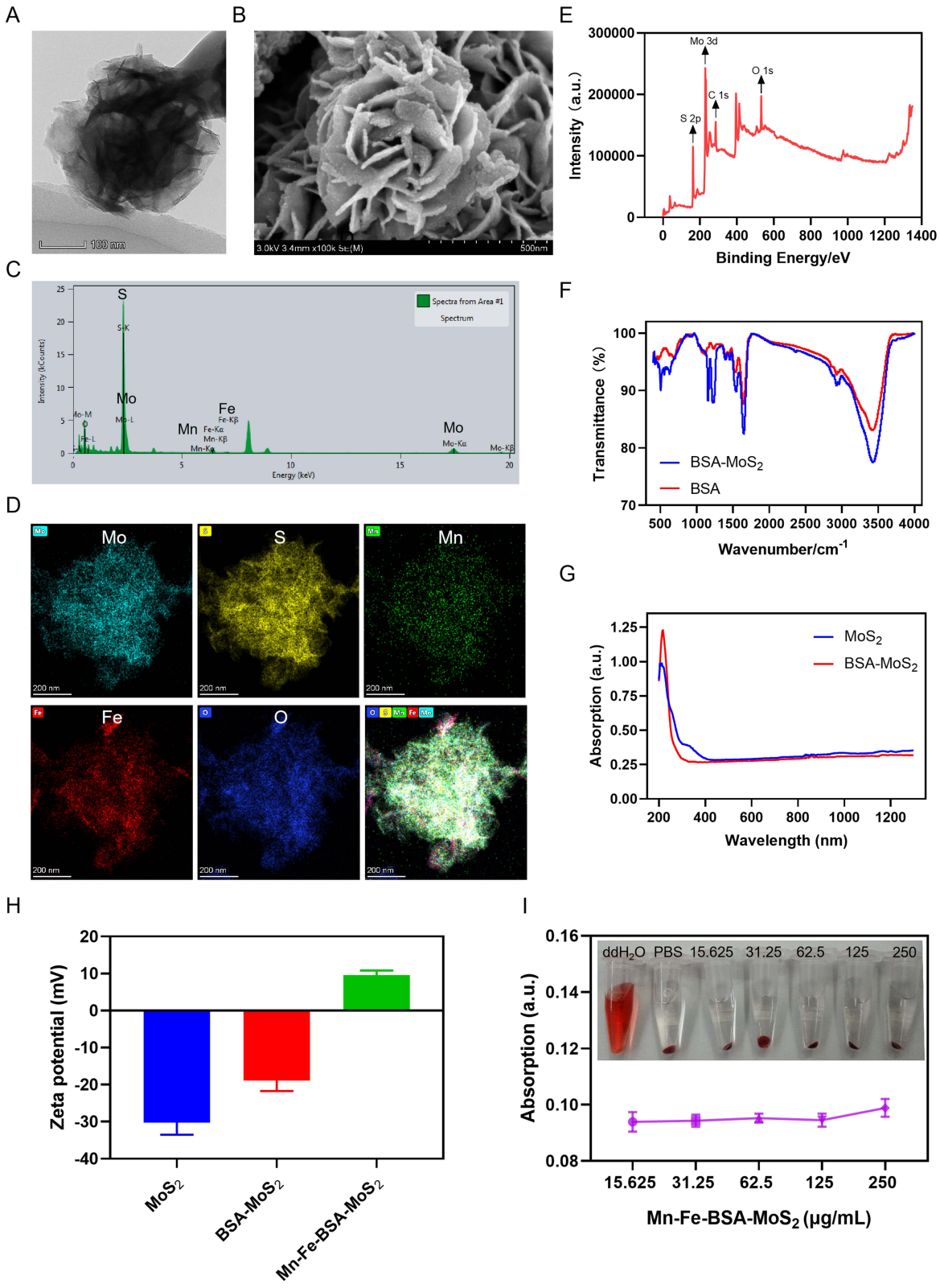

Figure 1 Synthesis and characterization of nanoflowers. (**A**) TEM images of BSA-MoS_2 nanoflowers. Scale bar: 100 nm. (**B**) SEM images of BSA-MoS_2 nanoflowers. Scale bar: 500 nm. (**C**) EDS Analysis of Mn-Fe-BSA-MoS_2 nanoflowers. (**D**) Elemental distribution mappings of Mn-Fe-BSA-MoS_2 nanoflowers. Scale bar: 200 nm. (**E**) XPS analysis of MoS_2 nanoflowers. (**F**) Fourier transform infrared spectroscopy analysis of BSA and BSA-MoS_2. (**G**) Absorption spectra of BSA-MoS_2 and MoS_2 aqueous solution. (**H**) Zeta potential of MoS_2, BSA-MoS_2 and Mn-Fe-BSA-MoS_2 nanoflowers. (**I**) Hemolysis rate of red blood cells incubated with Mn-Fe-BSA-MoS_2 at various concentrations (15.625, 31.25, 62.5, 125, 250 μg/mL), using deionized water and PBS as positive and negative controls, respectively.

https://doi.org/10.2147/IJN.S587614

characteristic peaks for Mo, S, C, and O, confirming the presence of these elements in the synthesized material. Fourier-transform infrared spectroscopy (FTIR) spectra displayed characteristic absorption peaks of BSA in the BSA-MoS_2 nanoflowers, confirming the successful coating of BSA on the MoS_2 surface (Figure 1F). The mechanism underlying the MWDT effect of MoS_2 nanoflowers may be related to plasmonic effects and ultraviolet light absorption. To investigate whether BSA coating affects the light absorption properties of MoS_2 nanoflowers, UV–Vis absorption spectroscopy was performed on both MoS_2 and BSA-MoS_2 nanoflowers (Figure 1G). The results showed that their light absorption profiles were nearly identical, suggesting that the BSA coating does not significantly alter the light absorption characteristics of the MoS_2 nanoflowers. Additionally, the zeta potential changed from −30.21±3.3 mV (MoS_2) to −18.86±2.88 mV (BSA-MoS_2) and further to 9.51±1.31 mV after Mn/Fe loading, indicating successful surface modification (Figure 1H). Hemolysis assays showed that Mn-Fe-BSA-MoS_2 nanoflowers caused negligible erythrocyte lysis across all tested concentrations, demonstrating excellent hemocompatibility (Figure 1I).

MWDT relies on the generation of high levels of ROS to induce tumor cell apoptosis and autophagy. However, the hypoxic conditions within tumor cells severely limit the efficacy of MWDT.[18] To address this challenge, we chelated Mn and Fe onto the surface of MoS_2 nanoflowers at a molar ratio of 2:1. The composite exhibits dual enzyme-mimicking activities, catalytically converting tumor-associated H_2O_2 into O_2 without consumption of Mn and Fe. The continuous supply of O_2 significantly boosts the generation of $^1O_2$ during MWDT. Furthermore, MWTT-induced vasodilation increases tumor blood flow and oxygenation, creating a positive feedback loop to amplify therapeutic efficacy.[14] Under MW irradiation, Mn-Fe-BSA-MoS_2 nanoflowers produced continuous O_2 in the presence of H_2O_2, whereas negligible oxygen generation was observed in PBS alone (Figure 2A). This indicates that the Mn-Fe-BSA-MoS_2 nanoflowers can effectively enhance O_2 generation under MW irradiation, thereby potentially improving the efficacy of MWDT in hypoxic tumor environments.

Doxorubicin (Dox) was employed as a chemotherapeutic agent to augment the anticancer efficacy of the nanoflowers.[30] In our synthesized Mn-Fe-Dox-BSA-MoS_2 nanoflowers, the drug loading capacity of Dox was determined to be approximately 80%. The cumulative release of Dox was less than 16% at pH 7.4 after 48 h, whereas it increased to approximately 42% under acidic conditions (pH 5.5). This marked difference is attributed to the protonation of the amino groups of Dox in the acidic environment, which enhances its hydrophilicity and thereby facilitates drug release. Consequently, the Mn-Fe-Dox-BSA-MoS_2 nanoflowers exhibit pH-responsive drug release properties, enabling preferential release of Dox in the acidic tumor microenvironment. This pH-sensitive release mechanism minimizes toxic side effects on normal cells while maximizing therapeutic efficacy at the tumor site. Furthermore, when Mn-Fe-Dox-BSA-MoS_2 nanoflowers were subjected to MW irradiation (8 W, 3 min) at specific time points, the Dox release rate surged to approximately 68% (Figure 2B and C). This observation indirectly confirms that the temperature elevation induced by MW irradiation substantially enhances the release of Dox from the nanoflowers.[31] This finding highlights the potential of combining MW irradiation with pH-responsive nanoflowers to achieve controlled and enhanced drug delivery in cancer therapy. The elemental composition and chemical states of the Mn-Fe-Dox-BSA-MoS_2 nanoflowers were analyzed by XPS. As shown in Figure S1, the survey spectrum reveals the presence of Mo, S, Mn, Fe, C, N, and O elements. The characteristic peaks of Mo 3d and S 2p confirm the existence of the MoS_2 framework. Meanwhile, the appearance of Mn 2p and Fe 2p peaks indicates the successful incorporation of Mn and Fe species into the MoS_2 nanoflowers. The N_2 adsorption-desorption isotherms of both pristine BSA-MoS_2 nanoflowers and Mn-Fe-Dox-BSA-MoS_2 nanoflowers are shown in Figure S2 and S3. Both samples exhibit typical type IV isotherms with a distinct H3 hysteresis loop and the Mn/Fe chelate-modified MoS_2 nanoflowers display a significantly higher nitrogen adsorption capacity than the pristine MoS_2 sample, as evidenced by the increased adsorption at high relative pressures ($P/P_0 > 0.8$). This suggests that the introduction of Mn/Fe chelates leads to an increase in the accessible surface area and pore volume. The specific surface areas calculated using the BET method were found to be 14.8367 m^2/g for pristine MoS_2 and 45.3963 m^2/g for Mn-Fe-Dox-BSA-MoS_2 nanoflowers. The average pore diameter of Mn-Fe-Dox-BSA-MoS_2 nanoflowers calculated by the BET method is 18.38 nm, while the BJH adsorption and desorption pore diameters are 23.77 nm and 17.33 nm, respectively, indicating a typical mesoporous structure.

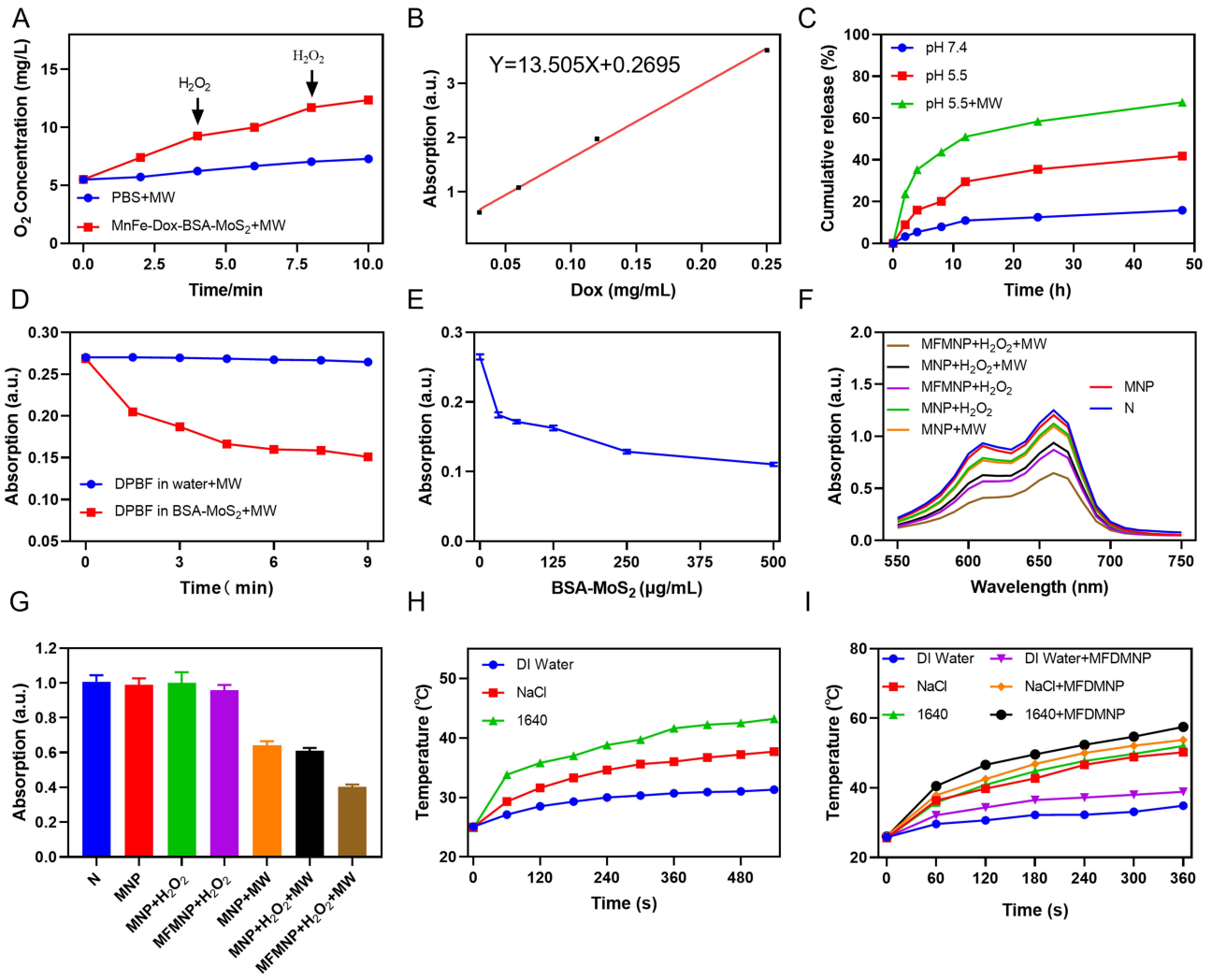

Figure 2 (**A**) Mn-Fe-Dox-BSA-MoS_2 nanoflowers produce dissolved oxygen under MW irradiation. (**B**) A calibration curve of Dox for the quantitation of its loading efficiency. (**C**) Release results of Dox in Mn-Fe-Dox-BSA-MoS_2 nanoflowers under different conditions. (**D**) Time dependent of $^1O_2$ generation by BSA-MoS_2 under microwave irradiation detected via the DPBF probes. (**E**) Concentration dependent of $^1O_2$ generation detected via the DPBF probes. (**F**) Generation of ·OH under different treatments was detected via the MB probes. (**G**) Generation of $^1O_2$ under different treatments detected via the DPBF probes. (**H**) Temperature changes of different aqueous suspension under microwave irradiation (5 W, 9 min). (**I**) Temperature changes of Mn-Fe-Dox-BSA-MoS_2 nanoflowers suspension at different aqueous suspension under microwave irradiation (8 W, 6 min).

Abbreviations: MNP, Dox-BSA-MoS_2 nanoflowers; MFDMNP, Mn-Fe-Dox-BSA-MoS_2 nanoflowers.

Potent Microwave Thermal and Dynamic Therapy of Nanoflowers

MWDT is a therapeutic strategy that relies on the generation of ROS to effectively induce tumor cell death.[32] Significant $^1O_2$ generation was observed from BSA-MoS_2 nanoflowers (at a concentration of 125 μg/mL) under MW irradiation, and the production increased with irradiation time (Figure 2D). Furthermore, as the concentration of BSA-MoS_2 nanoflowers increased under MW irradiation, the amount of $^1O_2$ generated showed a progressive rise (Figure 2E). These results demonstrate that the MoS_2 nanoflowers possess remarkable $^1O_2$ generation efficiency under MW irradiation, highlighting their significant potential for MWDT applications.

To further verify the impact of Mn and Fe ions on the MWDT performance of MoS_2, we measured the generation of ·OH and $^1O_2$ using MB and DPBF probes, respectively. Compared with the BSA-MoS_2+H_2O_2 group, the Mn-Fe-BSA-MoS_2+H_2O_2 group exhibited a higher yield of ·OH without MW irradiation, primarily due to the peroxidase-like activity of Mn-Fe-BSA-MoS_2 nanoflowers, which can catalyze the decomposition of H_2O_2 to generate ·OH. When the Mn-Fe-BSA-MoS_2+H_2O_2 group was subjected to MW irradiation, the production of ·OH further increased compared with the Mn-Fe-BSA-MoS_2+H_2O_2 group alone. This is likely attributed to the enhanced O_2 generation facilitated by Mn and Fe

ions, thereby amplifying the MWDT effect (Figure 2F). Similarly, we used the DPBF probe to evaluate the generation of $^1O_2$ by Mn-Fe-BSA-MoS_2 nanoflowers in the presence of H_2O_2 or MW irradiation. Compared with the BSA-MoS_2+MW and BSA-MoS_2+H_2O_2+MW groups, the Mn-Fe-BSA-MoS_2+H_2O_2+MW group showed a significantly higher yield of $^1O_2$. This enhancement is attributed to the elevated O_2 content resulting from Mn and Fe ion incorporation (Figure 2G).

The high temperature at the tumor site can effectively eradicate tumor cells, and MW irradiation inherently generates thermal energy. It would be even more advantageous if a selected nanomaterial possessed enhanced MW-responsive heating capability.[33] To this end, we systematically evaluated the thermosensitive properties of Mn-Fe-Dox-BSA-MoS_2 nanoflowers under MW irradiation. Initially, we examined temperature profiles of deionized water, NaCl solution, and 1640 culture medium under MW irradiation (5 W, 9 min). The results showed that the temperatures of the NaCl solution and 1640 solution increased significantly, likely due to the high-frequency collisions of ions caused by MW irradiation (Figure 2H). When the MW power was adjusted to 8 W, we observed a more pronounced thermal differential, with ionic solutions reaching substantially higher temperatures than pure water. Notably, incorporation of Mn-Fe-Dox-BSA-MoS_2 nanoflowers further amplified the heating effect across all media. The nanoflowers induced additional temperature increases of approximately 4 °C in deionized water, 3.5 °C in NaCl solution, and 5.5 °C in 1640 medium (Figure 2I). This enhanced temperature rise is likely attributed to the large specific surface area and interlayer structure of MoS_2 nanoflowers, which further promote the collision of manganese and iron ions and thereby amplify the heating effect.[28]

Nanoflowers Exhibit Potent Antitumor Effects in vitro

Efficient intracellular uptake of nanomaterials is a prerequisite for microwave-driven cancer cell ablation. To identify the optimal time window for subsequent cell experiments, we assessed the cellular phagocytosis of nanoflowers using immunofluorescence and flow cytometry. After co-incubating MB49 cells with DiI-labeled Mn-Fe-BSA-MoS_2 nanoflowers for 0.5 to 6 hours, distinct red fluorescence was observed within the cells, confirming successful nanoflowers uptake. To further verify whether the incorporation of Dox affects the cellular uptake rate, MB49 cells incubated with DiI-labeled Mn-Fe-Dox-BSA-MoS_2 nanoflowers for varying durations were analyzed by flow cytometry. The results revealed that the uptake rate peaked at 6 hours (Figure 3A and B). Additionally, bio-transmission electron microscopy (Bio-TEM) confirmed that MoS_2 nanoflowers were internalized into the cells, establishing a critical prerequisite for subsequent MWDT, MWTT, and chemotherapy to effectively eliminate tumor cells (Figure 3C).

In cell experiments, establishing the optimal concentration of nanoflowers is a critical first step. This concentration should be effective for therapeutic purposes while avoiding toxic effects on normal cells. To determine this, we initially incubated human umbilical vein endothelial (HUVEC) cells with various concentrations of Mn-Fe-BSA-MoS_2 nanoflowers for 24 hours and assessed cell viability using the CCK-8 assay. The results demonstrated that cell viability remained above 90% even at a concentration of 500 μg/mL, indicating that the nanoflowers exhibit negligible cytotoxicity to normal cells within this concentration range (Figure 3D). In contrast, when MB49 bladder cancer cells were co-incubated with different concentrations of Mn-Fe-BSA-MoS_2 nanoflowers for 24 hours, a significant reduction in cell viability was observed at 250 μg/mL (Figure 3E).

We ultimately selected a nanoflowers concentration of 125 μg/mL for subsequent experiments, which ensures both the safety of the nanoflowers and their efficacy in MWDT. To minimize the potential influence of microwave-induced thermal effects on MWDT evaluation, part of the cell viability experiments was conducted under ice-bath conditions during microwave irradiation, which effectively suppressed bulk temperature elevation while maintaining microwave exposure. The results indicated that MW irradiation alone, under ice-bath conditions, slightly inhibited cell viability, likely due to the generation of a small amount of ROS by MW irradiation. However, when BSA-MoS_2 nanoflowers were introduced, MW irradiation further decreased cell viability compared to the MW-only group, suggesting that microwave-activated ROS generation mediated by BSA-MoS_2 contributes to the cytotoxic effect beyond the thermal contribution. Moreover, the addition of Mn-Fe-BSA-MoS_2 nanoflowers led to an even greater decrease in cell viability upon MW irradiation. This enhancement is likely attributed to the catalytic synergy of Mn/Fe in promoting H_2O_2 decomposition into ·OH radicals and O_2, thereby augmenting the MWDT effect. Under standard temperature conditions, the combination of BSA-MoS_2 or Mn-Fe-BSA-MoS_2 nanoflowers with MW irradiation resulted in a more pronounced reduction in cell viability, indicating a synergistic contribution of MWDT and MWTT (Figure 3F).

https://doi.org/10.2147/IJN.S587614

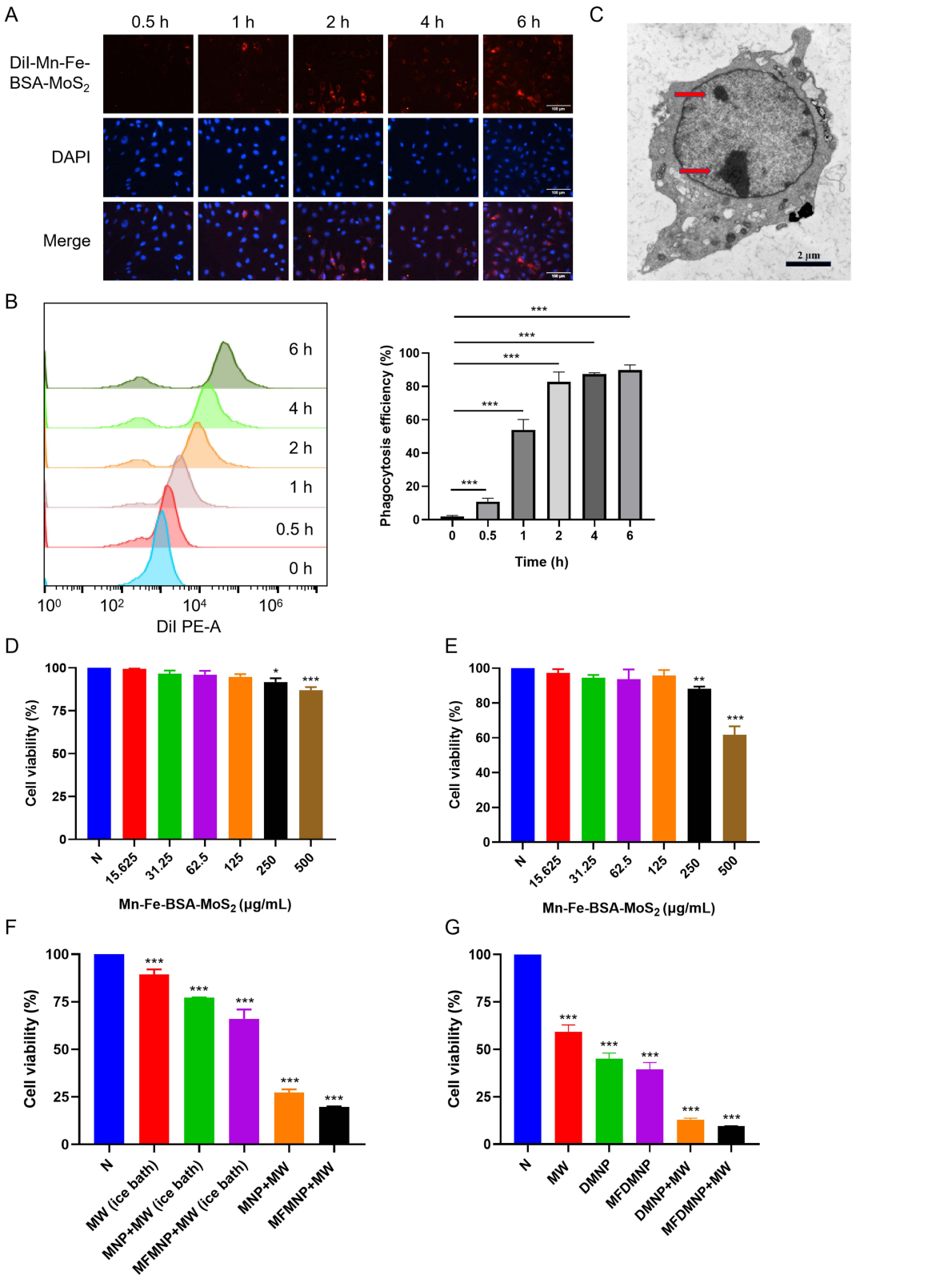

Figure 3 Cellular uptake and cell viability. (**A**) Intracellular uptake of Mn-Fe-BSA-MoS_2 nanoflowers labeled with DiI observed by fluorescence microscope after various intervals of incubation (scale bars: 100 μm). (**B**) Flow cytometry analysis of intracellular uptake of Mn-Fe-Dox-BSA-MoS_2 nanoflowers labeled with DiI. (**C**) Intracellular uptake of Mn-Fe-Dox-BSA-MoS_2 nanoflowers as observed by biological transmission electron microscopy. The red arrow indicates Mn-Fe-Dox-BSA-MoS_2 nanoflowers. (**D**) Activity of HUVEC cells after incubation with different concentrations of Mn-Fe-BSA-MoS_2 nanoflowers. (**E**) Activity of MB49 cells after intervention with different concentrations of Mn-Fe-BSA-MoS_2 nanoflowers. (**F**) Activity of MB49 cells following different Dox-free interventions via CCK8 assay. (**G**) Detection of survival rate of MB49 cells following various Dox-containing treatments by CCK8 assay. * indicates $p < 0.05$, ** indicates $p < 0.01$, *** indicates $p < 0.001$.
Abbreviations: DMNP, Dox-BSA-MoS_2 nanoflowers; MFDMNP, Mn-Fe-Dox-BSA-MoS_2 nanoflowers.

To explore the synergistic impact of MWTT and Dox on MB49 cell viability, cells were treated with Dox-loaded nanoflowers at room temperature. The findings revealed that MW therapy alone diminished cell viability by approximately 40%. Additionally, Dox chelated by BSA-MoS_2 nanoflowers reduced viability by about 55%, whereas Mn-Fe-Dox-BSA-MoS_2 nanoflowers maintained viability at nearly 40%. This improvement can be attributed to the enhanced efficacy of MWDT in conjunction with chemotherapy, which is facilitated by the incorporation of Mn/Fe. Notably, the combination of microwave radiation with Mn-Fe-Dox-BSA-MoS_2 nanoflowers further suppressed cell viability to around 10%, likely due to the synergistic amplification of both Dox cytotoxicity, MWTT and MWDT of the nanoflowers (Figure 3G).

What's more, to further investigate the effects of Dox chemotherapy combined with MWDT and MWTT on cells, we employed flow cytometry to quantitatively analyze ROS levels and apoptosis rates, and also observed the cell viability under various treatment conditions using live/dead staining methods. Our results demonstrated that even with MW irradiation alone at room temperature, a small amount of ROS was generated. Dox-BSA-MoS_2 nanoflowers can release Dox in the tumor microenvironment without MW irradiation, and Dox itself can induce ROS generation in tumor cells. Even in the absence of MW irradiation, the intrinsic peroxidase-like activity of Mn and Fe ions within Dox-BSA-MoS_2 nanoflowers contributed to additional ROS production. Notably, when Dox-BSA-MoS_2 nanoflowers were combined with MW irradiation, ROS levels were markedly increased, indicating that microwave activation of the nanoplatform promotes ROS generation while thermal effects may further potentiate the overall therapeutic outcome. This effect was further amplified by the catalytic activity of Mn and Fe ions (Figure 4A and B). MW irradiation inherently possesses thermal therapeutic effects, while BSA-MoS_2 nanoflowers, in addition to their MWDT capabilities, can further enhance the MWTT effect. Both MWDT and MWTT, along with Dox chemotherapy, promote apoptosis in tumor cells. Flow cytometry analysis revealed that the apoptosis rates in each group were consistent with the levels of ROS production. Specifically, the group treated with Mn-Fe-Dox-BSA-MoS_2 nanoflowers in combination with MW irradiation exhibited the most pronounced apoptotic response (Figures 4C and S4), suggesting a combinatorial effect of enhanced ROS generation and thermal potentiation.

To evaluate the cytotoxic effects of different interventions on MB49 cells, we used Calcein-AM and Propidium Iodide (PI) staining. Calcein-AM is a cell-permeable fluorescent dye that labels live cells, emitting green fluorescence under a fluorescence microscope, while PI stains dead cells by binding to their nuclei, producing red fluorescence. Compared with the control group, the MW-only group, Dox-BSA-MoS_2 group, and Mn-Fe-Dox-BSA-MoS_2 group all exhibited predominant green fluorescence with sporadic red signals, indicating that a small number of cells had undergone death. However, when MW irradiation was used to activate the therapeutic effects of MWDT and MWTT, complete fluorescence shifted from green to intense red. This observation suggested that the combination of MWDT, MWTT, and Dox chemotherapy significantly enhanced the cytotoxic effects on MB49 cells (Figure 4D). These results further validate the potent therapeutic efficacy of combining Dox chemotherapy with MWDT and MWTT, providing a solid foundation for the in vivo application of Mn-Fe-Dox-BSA-MoS_2 nanoflowers.

Verification of Excellent Biosafety in vivo

The potential toxicity of Mn-Fe-Dox-BSA-MoS_2 nanoflowers in mice is a crucial factor in determining their suitability as ideal materials for MWDT and MWTT. To comprehensively evaluate their in vivo biocompatibility, we performed histological examination on the heart, liver, spleen, lung, and kidney tissues of mice injected with Mn-Fe-Dox-BSA-MoS_2 nanoflowers solution. H&E staining of these tissues revealed no significant damage compared to the control group, indicating that the nanoflowers did not cause noticeable organ toxicity (Figure 5A). Additionally, comprehensive hematological analysis and blood biochemical profiling further confirmed the biosafety of Mn-Fe-Dox-BSA-MoS_2 nanoflowers, with all measured parameters (including liver/kidney function markers and complete blood counts) remaining within normal physiological ranges throughout the observation period (Figure 5B). These results indicate that the nanoflowers undergo efficient metabolic clearance through major detoxification pathways. They also demonstrate that the nanoflowers have excellent systemic biocompatibility at therapeutic doses and the selected dosage regimen maintains physiological homeostasis. To further investigate the pharmacokinetic profile of these nanoflowers, we performed serial blood collection via the facial vein at various time points post-injection and quantified molybdenum (Mo) concentrations. The results demonstrated a gradual decrease in Mo content over time, suggesting that the nanoflowers were effectively metabolized and cleared from the

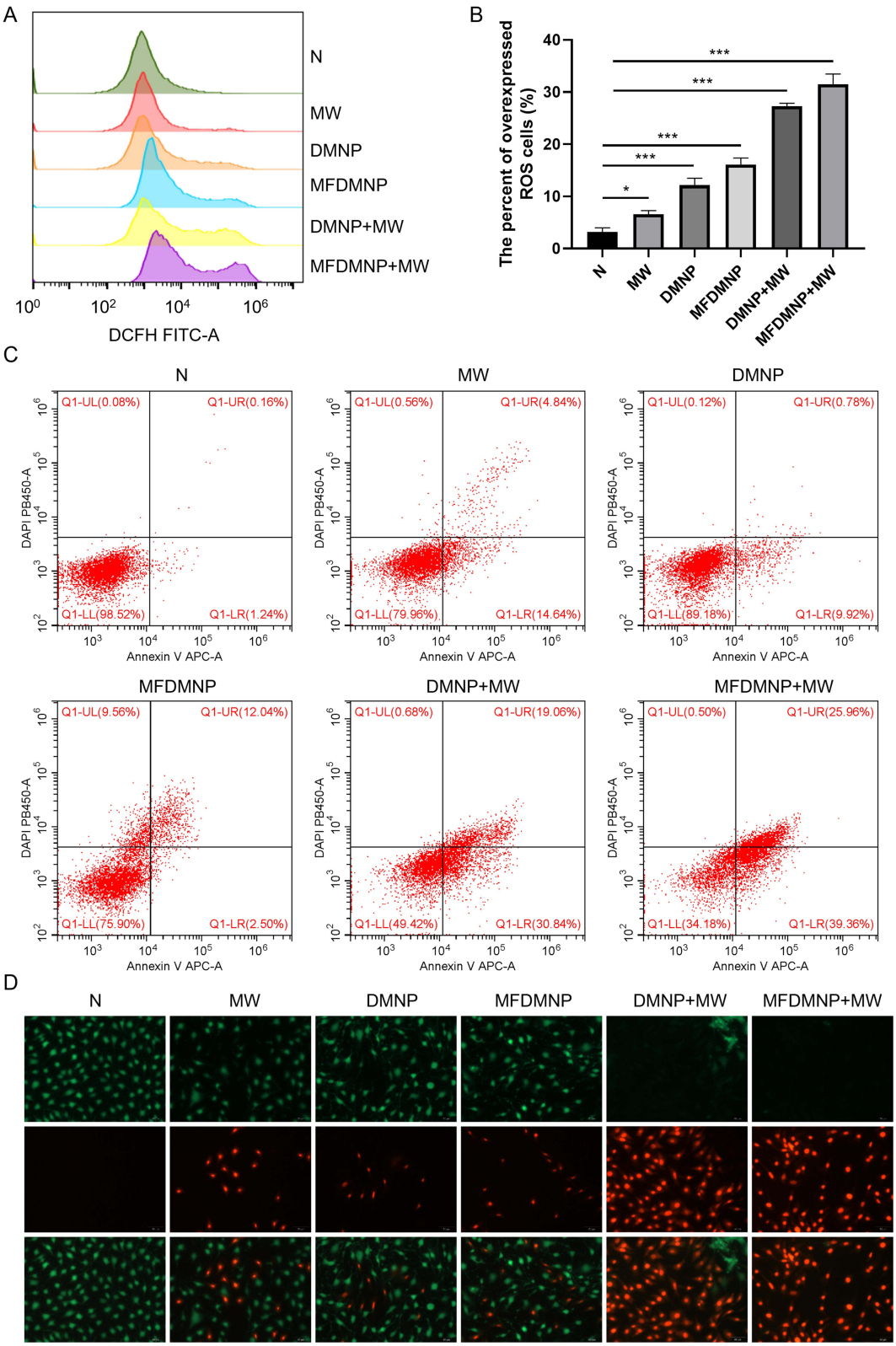

Figure 4 In vitro antitumor therapy. (**A**) ROS production in MB49 cells as determined by flow cytometry observation after different treatments. (**B**) Statistical analysis of ROS production in MB49 Cells under different treatments. Compared to the control group, * indicates $p < 0.05$, *** indicates $p < 0.001$. (**C**) Flow cytometry analysis of apoptosis after various treatments. (**D**) Live/dead cell staining after nanoflowers treatments in different groups (Scale bar: 50 μm).
Abbreviations: DMNP, Dox-BSA-MoS_2 nanoflowers; MFDMNP, Mn-Fe-Dox-BSA-MoS_2 nanoflowers.

https://doi.org/10.2147/IJN.S587614

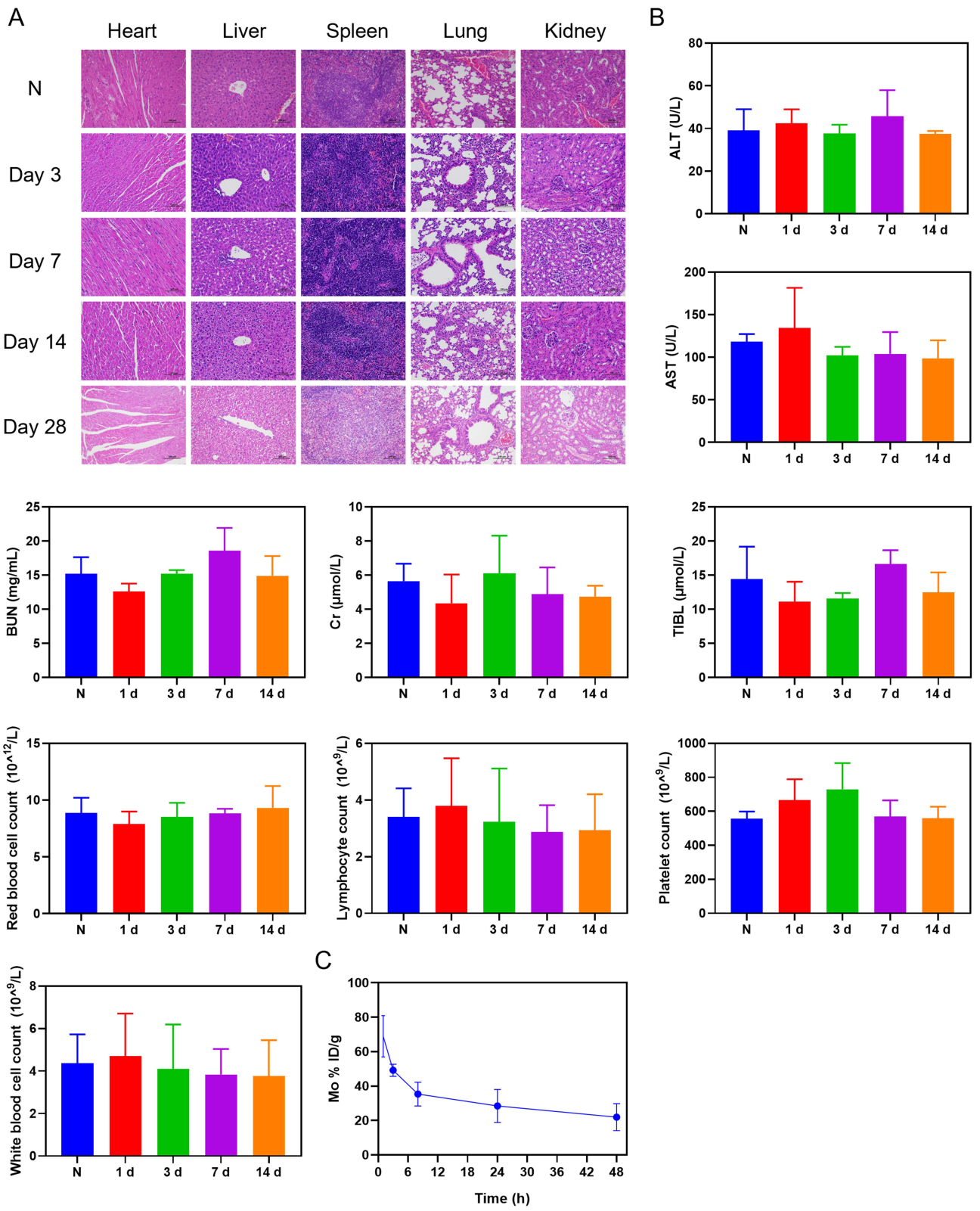

Figure 5 In vivo biosafety assessment. (**A**) H&E staining of the major organs at corresponding time intervals (scale bars: 100 μm). (**B**) No statistically significant differences were observed in blood routine and biochemical test of mice after intravenous administration of Mn-Fe-Dox-BSA-MoS_2. (**C**) Metabolism of Mo element in blood.

https://doi.org/10.2147/IJN.S587614

bloodstream (Figure 5C). This finding supports the biocompatibility and potential safety of Mn-Fe-Dox-BSA-MoS_2 nanoflowers for in vivo therapeutic applications.

Nanoflowers Enable Effective Multimodal Imaging in Tumor Detection

Nanomaterials with strong absorption of near-infrared light and efficient photothermal conversion capabilities are particularly valuable for photoacoustic (PA) imaging applications. Our studies demonstrate that Mn-Fe-Dox-BSA-MoS_2 nanoflowers exhibit excellent PA imaging properties, showing a concentration-dependent signal enhancement. Quantitative analysis revealed a linear relationship between PA signal intensity and nanoflower concentration across the tested range (0.0625–1 mg/mL) (Figure 6A). To evaluate the in vivo PA imaging potential of these nanoflowers, we conducted experiments in MB49 tumor-bearing nude mice. Following intravenous administration, ultrasound-guided PA imaging enabled precise tumor localization and longitudinal monitoring. The time-course analysis showed that tumor PA signals peaked at 6 hours post-injection, followed by gradual signal attenuation (Figures 6B and S5). These findings confirm that Mn-Fe-Dox-BSA-MoS_2 nanoflowers can serve as highly sensitive PA imaging agents, providing imaging support for monitoring the metabolic behavior of nanoflowers at the tumor site.

The Cy5.5 fluorescent dye is suitable for near-infrared fluorescence imaging due to its strong fluorescence properties and high photostability, which help minimize background interference in vivo and enhance the clarity and sensitivity of imaging.[34] Therefore, to further investigate the in vivo metabolism of the nanomaterial, we prepared Cy5.5-conjugated nanoflowers for fluorescence imaging to monitor their biodistribution. Cy5.5 fluorescent dye was conjugated to Mn-Fe-Dox-BSA-MoS_2 nanoflowers (Cy5.5-Mn-Fe-Dox-BSA-MoS_2), which were then intravenously injected into MB49 tumor-bearing mice via the tail vein. Fluorescence signals in the tumor region were monitored over a 24-hour period. The results demonstrated that the Cy5.5 signal intensity peaked within 6 h post-injection and gradually declined thereafter (Figure 6C). After 24 h, the mice were euthanized, and ex vivo fluorescence imaging was performed to quantify the signal distribution in major organs and tumor tissues (Figure 6D).

Nanoflowers Demonstrate Potent Anticancer Activity in vivo

MW irradiation inherently possesses thermal therapeutic effects. To evaluate the thermal therapy effects of MW irradiation alone and in combination with nanoflowers, we conducted real-time temperature monitoring at the tumor site during treatment. Our findings demonstrated that compared to the MW-only treatment group, the group treated with Mn-Fe-Dox-BSA-MoS_2 nanoflowers combined with MW irradiation exhibited a faster and more significant temperature increase at the tumor site, indicating a more effective microwave thermal therapy (Figure 6E and F).

To substantiate our findings that the triple-combination therapy (MWDT, MWTT, and Dox chemotherapy) provides maximal tumor suppression, we established a subcutaneous MB49 tumor model for comprehensive therapeutic evaluation. Once the tumor reached a standardized size (approximately 5 mm in diameter, rice grain equivalent), the mice were intravenously injected with the corresponding nanoflowers or an equivalent volume of PBS solution, followed by microwave irradiation according to the prescribed protocol (Figure 7A). Based on pharmacokinetic imaging data, we initiated microwave irradiation at the 6-hour post-injection timepoint for optimal nanoflowers accumulation. Compared with the control group, tumors in the Mn-Fe-Dox-BSA-MoS_2 group were smaller in size. MW irradiation alone exhibited moderate antitumor efficacy, primarily attributable to its inherent thermal effects. In comparison with the MW alone group, the Dox-BSA-MoS_2 combined with MW group showed superior antitumor effects, mainly attributed to ROS generation and microwave-induced heat facilitated further release of Dox under MW irradiation. The combined antitumor effect of MWDT, MWTT, and Dox chemotherapy was significantly superior to that of MW thermal therapy alone. The Mn-Fe-Dox-BSA-MoS_2 combined with MW group achieved the optimal antitumor efficacy, nearly eradicating the tumor completely. This enhanced therapeutic efficacy can be attributed not only to the synergistic combination of MWDT, MWTT, and Dox chemotherapy, but also to the tumor-localized O_2 generation catalyzed by Mn/Fe ions, which potentiates MWDT outcomes through improved tumor oxygenation (Figure 7B). Throughout the treatment process, no significant differences in body weight were observed among the groups, indirectly indicating the excellent biosafety profile of Mn-Fe-Dox-BSA-MoS_2 (Figure 7C). The tumor weights and volume from each group were measured after various treatments to further validate the therapeutic effects (Figures 7D and S6). We further confirmed the combined therapeutic effects by performing H&E, TUNEL, and PCNA staining on the subcutaneous tumors from each group (Figure 7E). The H&E staining results revealed

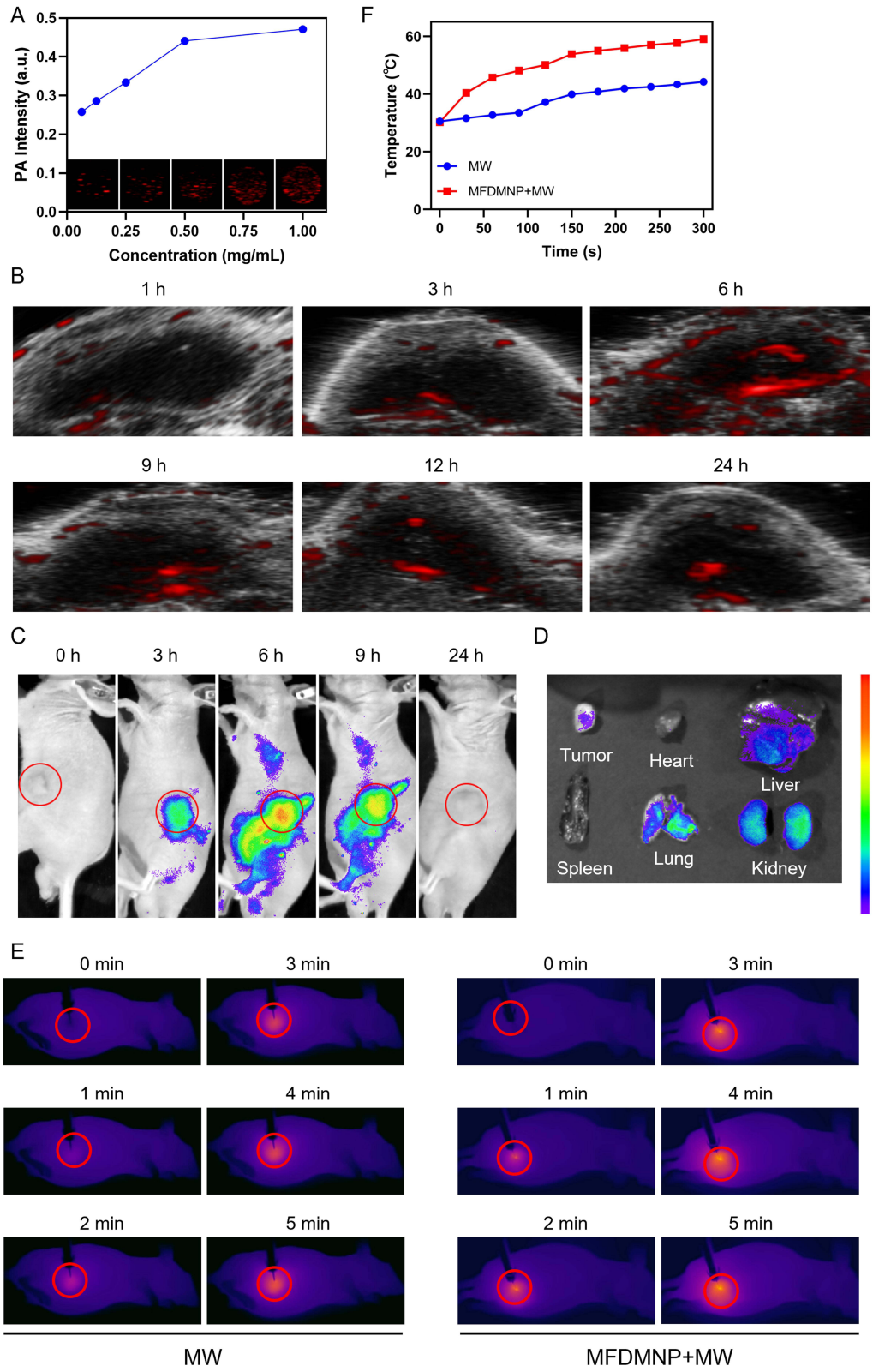

Figure 6 PA, near-infrared fluorescence and infrared thermal imaging in vitro and in vivo. (**A**) In vitro PA contrast images and PA values of Mn-Fe-Dox-BSA-MoS_2 nanoflowers at different concentrations. (**B**) In vivo PA images of tumors in tumor-bearing mice after intravenous injection of Mn-Fe-Dox-BSA-MoS_2 nanoflowers at different time points (1 mg/mL, 100 μL). (**C**) Near-infrared fluorescence images recorded at tumor region after intravenous injection of Cy5.5-Mn-Fe-Dox-BSA-MoS_2 at different time points. (**D**) Ex vivo fluorescence intensity of major organs and tumor tissue at 24 hours postinjection. (**E**) Infrared thermal image changes at tumor regions of different treatment group for 6 hours with MW irradiation (8 W, 5 minutes). (**F**) Temperature change curves at tumor regions of the different treatment group. The red circles delineate the areas occupied by the subcutaneous tumors in mice.
Abbreviation: MFDMNP, Mn-Fe-Dox-BSA-MoS_2 nanoflowers.

https://doi.org/10.2147/IJN.S587614

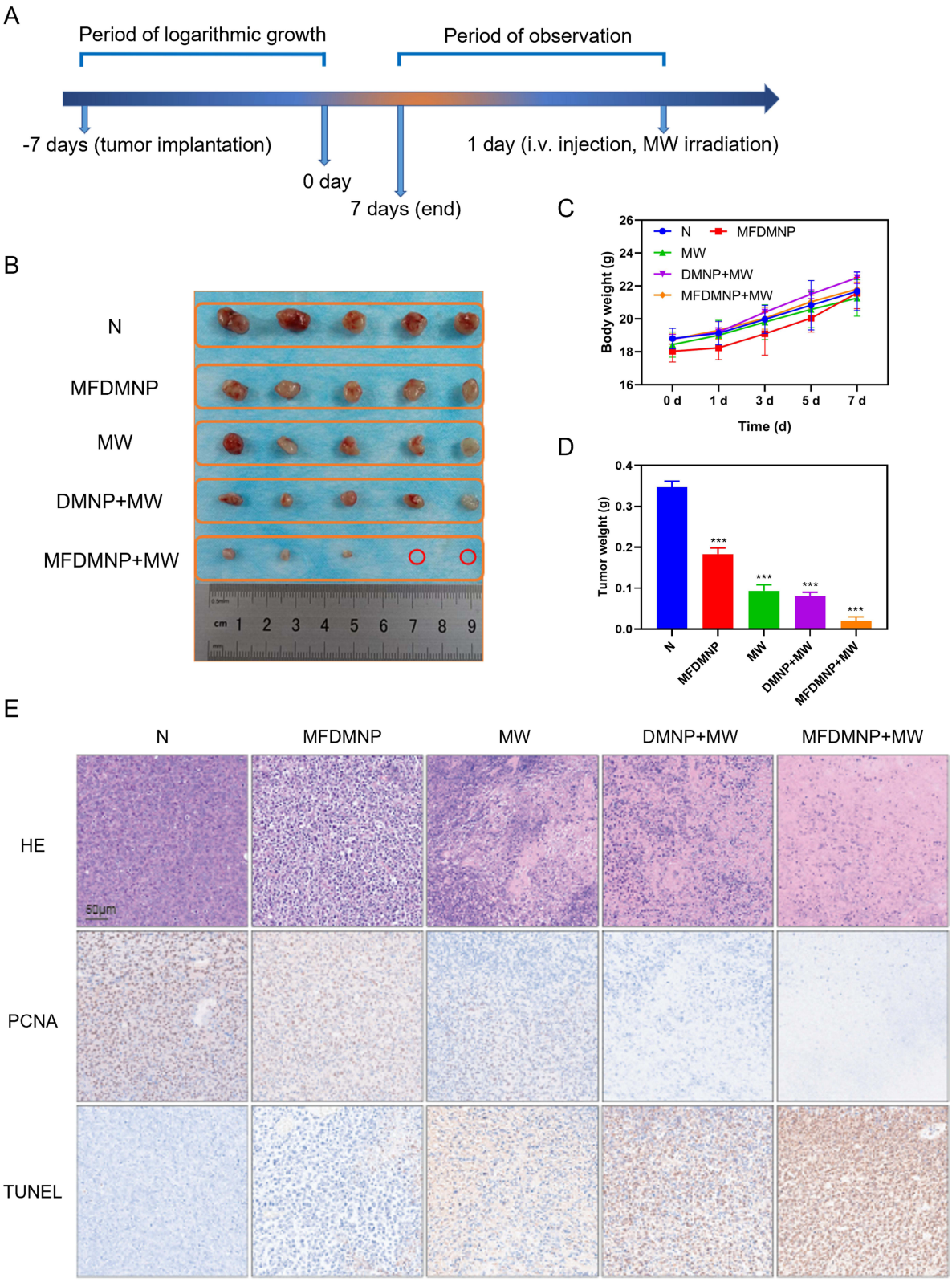

Figure 7 In vivo antitumor therapy. (**A**) Schematic illustration of the Mn-Fe-Dox-BSA-MoS_2 for primary tumor on BALB/c-nude mice. (**B**) Photographs of tumors dissected from mice of five groups after various treatments. The red circles represent complete elimination of the subcutaneous tumor in the mouse. (**C**) Time-dependent body weight curves of mice in the different groups. (**D**) Weight of tumors in the different groups. Compared to the control group, *** indicates $p < 0.001$. (**E**) H&E staining, PCNA staining and TUNEL staining of tumor sections from various treatment groups (scale bars: 50 μm).
Abbreviations: DMNP, Dox-BSA-MoS_2 nanoflowers; MFDMNP, Mn-Fe-Dox-BSA-MoS_2 nanoflowers.

that the group treated with Mn-Fe-Dox-BSA-MoS_2 nanoflowers combined with MW irradiation exhibited significantly more pronounced nuclear pyknosis, karyolysis, and karyorrhexis compared to other groups, indicating the most severe tumor cell necrosis and the best therapeutic effect. The TUNEL assay and PCNA staining were used to evaluate apoptosis and proliferation of tumor cells, respectively. The Dox-BSA-MoS_2 nanoflowers combined with MW irradiation resulted in a significant increase in apoptotic cells and a decrease in proliferating cells compared to the first three groups. The group treated with Mn-Fe-Dox-BSA-MoS_2 nanoflowers combined with MW irradiation exhibited even more apoptosis and stronger proliferation suppression than the Dox-BSA-MoS_2 plus MW group. This was mainly due to the improved tumor hypoxia microenvironment, which further enhanced the combined therapeutic effects.

Limitations of the Study

Despite the promising therapeutic outcomes demonstrated in this study, several limitations remain. First, the long-term biodistribution and metabolic pathways of Mn-Fe-Dox-BSA-MoS_2 nanoflowers require further investigation. Second, although the subcutaneous tumor model provides preliminary evidence of therapeutic efficacy, orthotopic bladder cancer models may better simulate the clinical tumor microenvironment. Future studies should also explore the potential immunological effects of microwave-induced tumor ablation combined with nanotherapy.

Conclusions

We developed microwave-responsive Mn-Fe-Dox-BSA-MoS_2 nanoflowers using MoS_2 as a carrier to load Dox and chelate Mn/Fe ions, forming a multifunctional nanoplatform. The 3D BSA-MoS_2 structure enhanced microwave energy absorption and ROS generation for microwave dynamic/thermal therapy, while Mn and Fe ions catalyzed H_2O_2 decomposition to produce O_2 and relieve tumor hypoxia, thereby improving therapeutic efficacy. Additionally, the nanoflowers enabled targeted Dox delivery and real-time PA/fluorescence imaging, achieving synergistic tumor therapy and imaging guidance.

Acknowledgments

The authors are grateful to the State Key Laboratory of Ultrasound in Medicine and Engineering for providing experimental equipment and facilities. This paper has been uploaded to ResearchGate as a preprint: https://www.researchgate.net/publication/394535882_Microwave-Responsive_Mnfe-Based_Molybdenum_Disulfide_Nanoflowers_for_Enhanced_Thermal-Dynamic-Chemo_Synergisti_Therapy_in_Bladder_Cancer.

Funding

This work was supported by the Natural Science Foundation of Zhejiang Province (Grant No. LTGY24H160005), China Postdoctoral Science Foundation (Grant No. 2021MD703925), Chongqing Postdoctoral Research Special Funding Project (Grant No. 2112012723387098), the Program for Youth Innovation in Future Medicine at Chongqing Medical University (Grant No.W0170), Natural Science Foundation of Ningbo Municipality (Grant No. 2022J218, 2022J217, and 2023J018), Ningbo Public Welfare Science and Technology Project (Grant No. 2023Y11), Zhejiang Provincial Foundation for Medical and Health Sciences (Grant No.2024KY305, 2024KY1514 and 2025HY0908), Ningbo Public Welfare Technology Research Program (Grant No.2023S025), Basic Research Project of Shanxi Province (Grant No. 20210302123259), Doctoral Research Project of Shanxi Medical University (Grant No. XD1901) and the Ningbo Top Medical and Health Research Program (Grant No. 2022020203).

Disclosure

The authors declare that they have no competing interests.

References

1. Sung H, Ferlay J, Siegel RL, et al. Global cancer statistics 2020: GLOBOCAN estimates of incidence and mortality worldwide for 36 cancers in 185 countries. *CA Cancer J Clin*. 2021;71(3):209–249. doi:10.3322/caac.21660
2. Jubber I, Ong S, Bukavina L, et al. Epidemiology of bladder cancer in 2023: a systematic review of risk factors. *Eur Urol*. 2023;84(2):176–190. doi:10.1016/j.eururo.2023.03.029

3. Yi L, Ai K, Li X, Li Z, Li Y. Bone metastasis in bladder cancer. *J Pers Med*. 2022;13(1):54. doi:10.3390/jpm13010054
4. Lopez-Beltran A, Cookson MS, Guercio BJ, et al. Advances in diagnosis and treatment of bladder cancer. *BMJ*. 2024;12(384):e076743. doi:10.1136/bmj.2023-076743
5. Babjuk M, Burger M, Capoun O, et al. European association of urology guidelines on non-muscle-invasive bladder cancer (Ta, T1, and Carcinoma in Situ). *Eur Urol*. 2022;81(1):75–94. doi:10.1016/j.eururo.2021.08.010
6. Russo GI, Sholklapper TN, Cocci A, et al. Performance of Narrow Band Imaging (NBI) and Photodynamic Diagnosis (PDD) fluorescence imaging compared to White Light Cystoscopy (WLC) in detecting non-muscle invasive bladder cancer: a systematic review and lesion-level diagnostic meta-analysis. *Cancers*. 2021;13(17):4378. doi:10.3390/cancers13174378
7. Khetrapal P, Wong JKL, Tan WP, et al. Robot-assisted radical cystectomy versus open radical cystectomy: a systematic review and meta-analysis of perioperative, oncological, and quality of life outcomes using randomized controlled trials. *Eur Urol*. 2023;84(4):393–405. doi:10.1016/j.eururo.2023.04.004
8. Clements MB, Atkinson TM, Dalbagni GM, et al. Health-related quality of life for patients undergoing radical cystectomy: results of a large prospective cohort. *Eur Urol*. 2022;81(3):294–304. doi:10.1016/j.eururo.2021.09.018
9. Jain P, Kathuria H, Momin M. Clinical therapies and nano drug delivery systems for urinary bladder cancer. *Pharmacol Ther*. 2021;226:107871. doi:10.1016/j.pharmthera.2021.107871
10. Wang B, Hu S, Teng Y, et al. Current advance of nanotechnology in diagnosis and treatment for malignant tumors. *Signal Transduct Target Ther*. 2024;9(1):200. doi:10.1038/s41392-024-01889-y
11. Guo Q, Tang Y, Wang S, Xia X. Applications and enhancement strategies of ROS-based non-invasive therapies in cancer treatment. *Redox Biol*. 2025;80:103515. doi:10.1016/j.redox.2025.103515
12. Yu X, Lyu M, Ou X, et al. AIEgens/mitochondria nanohybrids as bioactive microwave sensitizers for non-thermal microwave cancer therapy. *Adv Healthc Mater*. 2023;12(12):e2202907. doi:10.1002/adhm.202202907
13. Wang Y, Ren X, Zheng Y, et al. Boosting microwave thermo-dynamic cancer therapy of TiMOF via COF-coating. *Small*. 2023;19(49):e2304440. doi:10.1002/smll.202304440
14. Pandey NK, Xiong W, Wang L, et al. Aggregation-induced emission luminogens for highly effective microwave dynamic therapy. *Bioact Mater*. 2022;7:112–125. doi:10.1016/j.bioactmat.2021.05.031
15. Ding WZ, Wei H, Wu JP, et al. Liver cirrhosis and tumor location can affect the range of intrahepatic microwave ablation zone. *Int J Hyperthermia*. 2023;40(1):2181843. doi:10.1080/02656736.2023.2181843
16. Zeng Z, Fu C, Sun X, et al. Reversing the immunosuppressive microenvironment with reduced redox level by microwave-chemo-immunostimulant Ce-Mn MOF for improved immunotherapy. *J Nanobiotechnology*. 2022;20(1):512. doi:10.1186/s12951-022-01699-w
17. Xu X, Wu Q, Tan L, Men X, Huang Y, Li H. Biomimetic metal-chalcogenide agents enable synergistic cancer therapy via microwave thermal-dynamic therapy and immune cell activation. *ACS Appl Mater Interfaces*. 2023;15(36):42182–42195. doi:10.1021/acsami.3c05728
18. Wu Q, Yu Y, Yu X, et al. Engineering liquid metal-based nanozyme for enhancing microwave dynamic therapy in breast cancer PDX model. *J Nanobiotechnology*. 2023;21(1):399. doi:10.1186/s12951-023-02121-9
19. Li S, Chen Z, Tan L, et al. MOF@COF nanocapsule for the enhanced microwave thermal-dynamic therapy and anti-angiogenesis of colorectal cancer. *Biomaterials*. 2022;283:121472. doi:10.1016/j.biomaterials.2022.121472
20. Sasanipoor F, Zhang Z. Molybdenum disulfide nanocomposites for cancer diagnosis and therapeutics: biosensors, bioimaging, and phototherapy. *Adv Healthc Mater*. 2025;14(14):e2500655. doi:10.1002/adhm.202500655
21. Jin L, Zheng Y, Liu X, et al. Magnetic composite rapidly treats staphylococcus aureus-infected osteomyelitis through microwave strengthened thermal effects and reactive oxygen species. *Small*. 2022;18(41):e2204028. doi:10.1002/smll.202204028
22. Wang J, Sui L, Huang J, et al. MoS_2-based nanocomposites for cancer diagnosis and therapy. *Bioact Mater*. 2021;6(11):4209–4242. doi:10.1016/j.bioactmat.2021.04.021
23. Jin L, Wu S, Mao C, et al. Rapid and effective treatment of chronic osteomyelitis by conductive network-like MoS2/CNTs through multiple reflection and scattering enhanced synergistic therapy. *Bioact Mater*. 2024;31:284–297. doi:10.1016/j.bioactmat.2023.08.005
24. Yu X, Xu C, Sun J, et al. Recent developments in two-dimensional molybdenum disulfide-based multimodal cancer theranostics. *J Nanobiotechnology*. 2024;22(1):515. doi:10.1186/s12951-024-02785-x
25. Wen L, Liu H, Hu C, et al. Thermoacoustic imaging-guided thermo-chemotherapy for hepatocellular carcinoma sensitized by a microwave-responsive nitric oxide nanogenerator. *ACS Appl Mater Interfaces*. 2023;15(8):10477–10491. doi:10.1021/acsami.2c22523
26. Kuerban K, Gao X, Zhang H, et al. Doxorubicin-loaded bacterial outer-membrane vesicles exert enhanced anti-tumor efficacy in non-small-cell lung cancer. *Acta Pharm Sin B*. 2020;10(8):1534–1548. doi:10.1016/j.apsb.2020.02.002
27. Saharkhiz S, Zarepour A, Zarrabi A. A new theranostic pH-responsive niosome formulation for doxorubicin delivery and bio-imaging against breast cancer. *Int J Pharm*. 2023;637:122845. doi:10.1016/j.ijpharm.2023.122845
28. Wu Q, Tan L, Ren X, et al. Metal-organic framework-based nano-activators facilitating microwave combined therapy via a divide-and-conquer tactic for triple-negative breast cancer. *ACS Nano*. 2023;17(24):25575–25590. doi:10.1021/acsnano.3c09734
29. Hsu WH, Ku CL, Lai YR, Wang SSS, Chou SH, Lin TH. Developing targeted drug delivery carriers for breast cancer using glutathione-sensitive doxorubicin-coupled glycated bovine serum albumin nanoparticles. *Int J Biol Macromol*. 2023;249:126114. doi:10.1016/j.ijbiomac.2023.126114
30. Xu HZ, Li TF, Wang C, et al. Synergy of nanodiamond-doxorubicin conjugates and PD-L1 blockade effectively turns tumor-associated macrophages against tumor cells. *J Nanobiotechnology*. 2021;19(1):268. doi:10.1186/s12951-021-01017-w
31. Cardoso BD, Rodrigues ARO, Bañobre-López M, et al. Magnetoliposomes based on shape anisotropic calcium/magnesium ferrite nanoparticles as nanocarriers for doxorubicin. *Pharmaceutics*. 2021;13(8):1248. doi:10.3390/pharmaceutics13081248
32. Zhou H, Liu Z, Zhang Z, et al. Copper-cysteamine nanoparticle-mediated microwave dynamic therapy improves cancer treatment with induction of ferroptosis. *Bioact Mater*. 2023;24:322–330. doi:10.1016/j.bioactmat.2022.12.023
33. Luo X, Sun HY, Lu SY, et al. Fe-doped Cu-based bimetallic metal-organic frameworks as nanoscale microwave sensitizers for enhancing microwave thermal and dynamic therapy for hepatocellular carcinoma. *Nanoscale*. 2024;16(23):11069–11080. doi:10.1039/d4nr00654b
34. Luo M, Yukawa H, Sato K, et al. Multifunctional magnetic CuS/Gd2O3 nanoparticles for fluorescence/magnetic resonance bimodal imaging-guided photothermal-intensified chemodynamic synergetic therapy of targeted tumors. *ACS Appl Mater Interfaces*. 2022;14(30):34365–34376. doi:10.1021/acsami.2c06503